Chapter 2

Equivalent electrical circuit of 1-D TiO_2 nanostructures-based sensor using impedance analysis

2. 1 Introduction

Sensors using nanostructured metal oxides were reported extensively for different gases and vapors as discussed in Chapter 1. The sensing mechanism of these sensors was relied on tracking either resistance or capacitance of the sensor in air and target VOC ambient [1-12]. However, a combined study of both resistive and capacitive properties of the nanostructured metal oxide-based sensor is relatively less investigated. Considering the individual importance of both resistive and capacitive mode of sensing, the current study is focused on identifying resistive and capacitive components of the sensor separately. For this, a 1-D TiO_2 nanostructures-based sensor was fabricated and characterized by using impedance analysis.

1-D nanostructure of TiO_2 was obtained by synthesizing highly ordered 1-D TiO_2 nanotubes array using electrochemical anodization technique and a sandwich/vertical structure device i.e., Au/TiO_2 nanotubes/Ti was used as a test device. A considerable effort was given to characterize individual resistive and capacitive components of the sensing layer of sensor. For this, impedance of the sensor was measured for a wide range of frequency with different temperature, vacuum level and reducing vapor ambient. Also, an equivalent electrical circuit model of the sensor was proposed using Cole-Cole plots obtained from the experimental results. Afterward, the structural and morphological properties of TiO_2 nanostructure were co-related with the resistive and capacitive response of the sensor. Thus, these parameters can be tuned accordingly making the sensor suitable for preferentially sensing either in resistive or in capacitive mode.

2. 2 Fabrication of 1-D TiO_2 nanostructure-based sensor

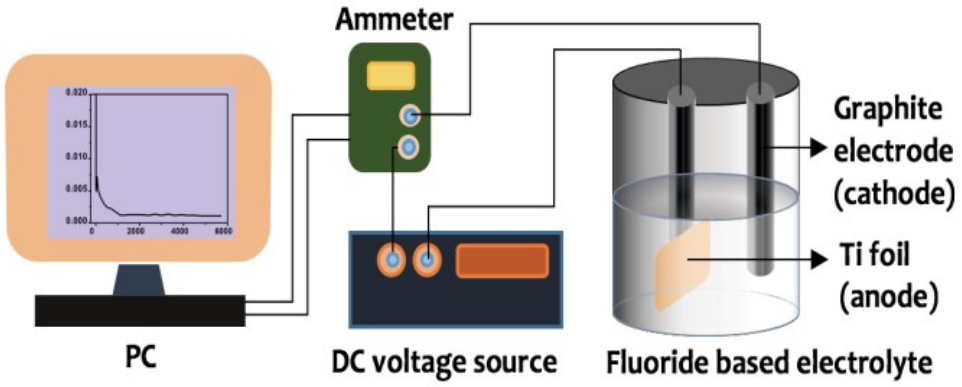

Fig. 2.1 Electrochemical anodization setup for the synthesis of TiO_2 nanotubes

TiO_2 nanotubes were synthesized by using electrochemical anodization of Ti foil (99.99% purity, and 0.25 mm thick) in a two-electrodes configuration where anode was of Ti foil (25 mm × 25 mm) and cathode was of graphite rod (20 mm dia., 25 mm length inside the electrolyte). A schematic of the anodization setup is shown in Fig. 2.1. Anodization was carried out at 27 °C for 90 minutes by applying a constant DC bias voltage of 40 V through Keysight E3643A. The electrolyte was made up of 0.5 wt.% NH_4F, 10 vol.% deionized (DI) water and ethylene glycol. The content of electrolyte primarily decides whether the grown oxide layer will be porous or compact. The growth mechanism of TiO_2 nanotubes can be described by using the following chemical equations (eq. (2.1-2.6)) [13]:

$$Ti \rightarrow Ti^{4+} + 4e^- \tag{2.1}$$

$$Ti + 2H_2O \rightarrow TiO_2 + 4H^+ + 4e^- \tag{2.2}$$

$$Ti^{4+} + 2H_2O \rightarrow TiO_2 + 4H^+ \tag{2.3}$$

$$4H_2O + 4e^- \rightarrow 2H_2 + 4OH^- \tag{2.4}$$

$$TiO_2 + 6F^- + 4H^+ \rightarrow [TiF_6]^{2-} + 2H_2O \tag{2.5}$$

$$Ti^{4+} + 6F^- \rightarrow [TiF_6]^{2-} \tag{2.6}$$

Initially, a uniform oxide layer was grown by field assisted oxidation of Ti substrate as represented in eq. (2.1-2.3). Also, H_2 evolution took place at cathode according to eq. 2.4. After the initial growth of oxide layer, competition and equilibrium between two processes namely, field assisted oxidation and dissolution, gave rise to the formation of TiO_2 nanotubes. Oxidation process involved diffusion of O^{2-} ions through the oxide layer where it interact with Anode (Ti metal) to form TiO_2. Subsequently, Ti^{4+} ions released from Anode diffused towards electrolyte. Now, HF present in the electrolyte attacked the TiO_2 layer which resulted in the formation of a soluble $[TiF_5]^{2-}$ complex as shown in eq. (2.5). Also, Ti^{4+} ions react with F^- ions to form a soluble $[TiF_6]^{2-}$ as shown in eq. (2.6). Now, the following three possibilities may arise depending upon concentrations of F^- ions in the electrolyte:

i. If F^- ions concentration is large, then Ti^{4+} ions get continuously dissolve by F^- in the electrolyte (eq. 2.5) and hence, no oxide layer will grow.

ii. If F^- ions concentration is less, then Ti^{4+} ions do not get dissolve completely by F^- and hence, a stable metal oxide layer will grow.

iii. If F^- ions concentration is moderate, then completion between oxidation and dissolution of Ti^{4+} will lead to form a porous oxide layer.

In the above experiment, a moderate concentration of HF was taken and thus, the oxide layer started to etch and pores were created in oxide layer. These pores start to compete with each other for available current (due to applied electric field) and self-ordering conditions get established under steady state conditions which results in nanotubes like morphology of oxide layer.

After the successful formation of TiO_2 nanotubes over Ti metal substrate, samples were thoroughly cleaned with DI water followed by ethanol. Afterward, the TiO_2 nanotubes/Ti samples were annealed in air ambient for 4 h at 330 °C. An optimum annealing temperature of 330 °C was used so that the anatase phase should not convert into the rutile phase. For gas sensing applications, the gas sensor needs to be stable in terms of its resistance and capacitive values. As-synthesized TiO_2 nanotubes are seldom

used in gas sensing because of its unstable nature. Annealing was required in this experiment to increase the crystallinity and mechanical strength of the TiO_2 nanotubes [14]. For top electrode contact, Au film (1 mm × 1 mm × 100 nm) was deposited over TiO_2 nanotubes/Ti sample (2 mm × 7 mm) by thermal evaporation technique. Cu metal mask (1 mm × 1 mm) was used to wrap TiO_2 nanotubes/Ti sample which resulted in the selective deposition of Au during thermal evaporation process. After the deposition of Au thin film, TiO_2 nanotubes array was fractionally etched (1.5 mm) by HF solution to get the bare Ti surface. Ti substrate and top Au layer act as the bottom and top electrodes, respectively. Conducting Ag paste was used to connect Cu wires with both Au and Ti contacts.

2. 3 Experimental setup for measuring impedance of the sensor

Fig. 2.2 shows the schematic of sensing setup employed for static mode testing. The sensor was placed inside a 500 ml glass test chamber with an air inlet and outlet valve. Two contacts of Au and Ti from the sensor were connected to an LCR meter (GWInstek 6300) using Cu wires. Air flow inside the test chamber was controlled with a mass flow controller (MFC). The test chamber was placed inside a heating mantle for realizing different temperature ambient. For different vacuum levels, the closed chamber ambient was pumped down to a pressure of ~650 mm Hg and the pressure further decreased qualitatively with the duration of pumping (maximum 90 min). For studying VOC sensing properties of the sensor, a fixed amount of test VOC (V_1 in μL) was injected through the opening valve into the glass chamber using a micro-syringe (Hamilton 1710RN SYR). The concentration of VOC in glass chamber was calculated as C (ppm) = $2.46 \times (V_1D/VM) \times 10^3$, where, D (gm/mL), V (l), and M (gm/mol) represent density of VOC, volume of the test chamber, and molecular weight of VOC respectively [15]. After getting saturated response, the outlet valve of the test chamber was opened for recovery or to achieve the initial baseline resistance and capacitance values of the sensor. For impedance analysis of the sensor, real and imaginary

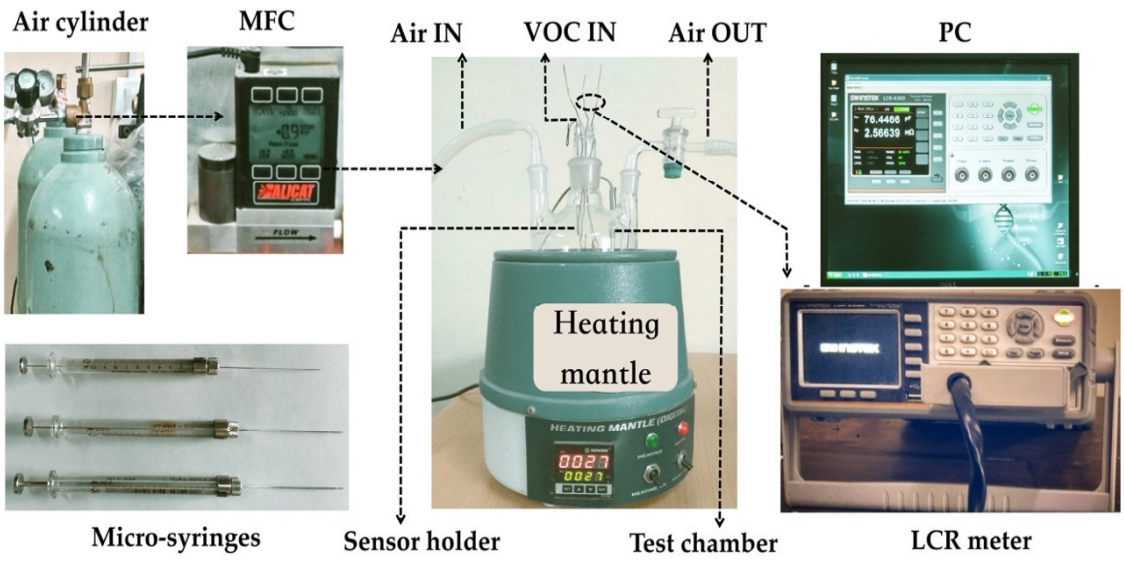

Fig. 2.2 A schematic showing sensing set-up via injection method.

components of impedance of the sensor was measured under various temperature, vacuum level and reducing vapor ambient. Resistive response magnitude (RRM) and capacitive response magnitude (CRM) of the sensor were calculated using eq. (2.7) and (2.8), respectively as given below:

$$\mathrm{RRM} = \frac{R_a - R_v}{R_a} \times 100 \tag{2.7}$$

$$\mathrm{CRM} = \frac{C_v - C_a}{C_a} \times 100 \tag{2.8}$$

Where, R_a and R_v denote resistance of the sensor in air and vapor ambient, respectively. C_a and C_v denote capacitance of the sensor in air and vapor ambient, respectively.

2. 4 Equivalent electrical circuit of the sensor

Fig. 2.3 (a) and (b) present the side and top view of the sandwich structure-based device. A simplified side view of the sensor device is represented in Fig. 2.3 (c) and a corresponding circuit model of Au/TiO_2nanotubes/Ti device is also represented in Fig. 2.3 (d). The various resistive components of sensor device such as R_X, R_{CA} and R_{CT} were originated from TiO_2 nanotubes array, Au/TiO_2, and Ti/TiO_2 junctions, respectively. Similarly, the capacitive components C_A and C_B were originated from the

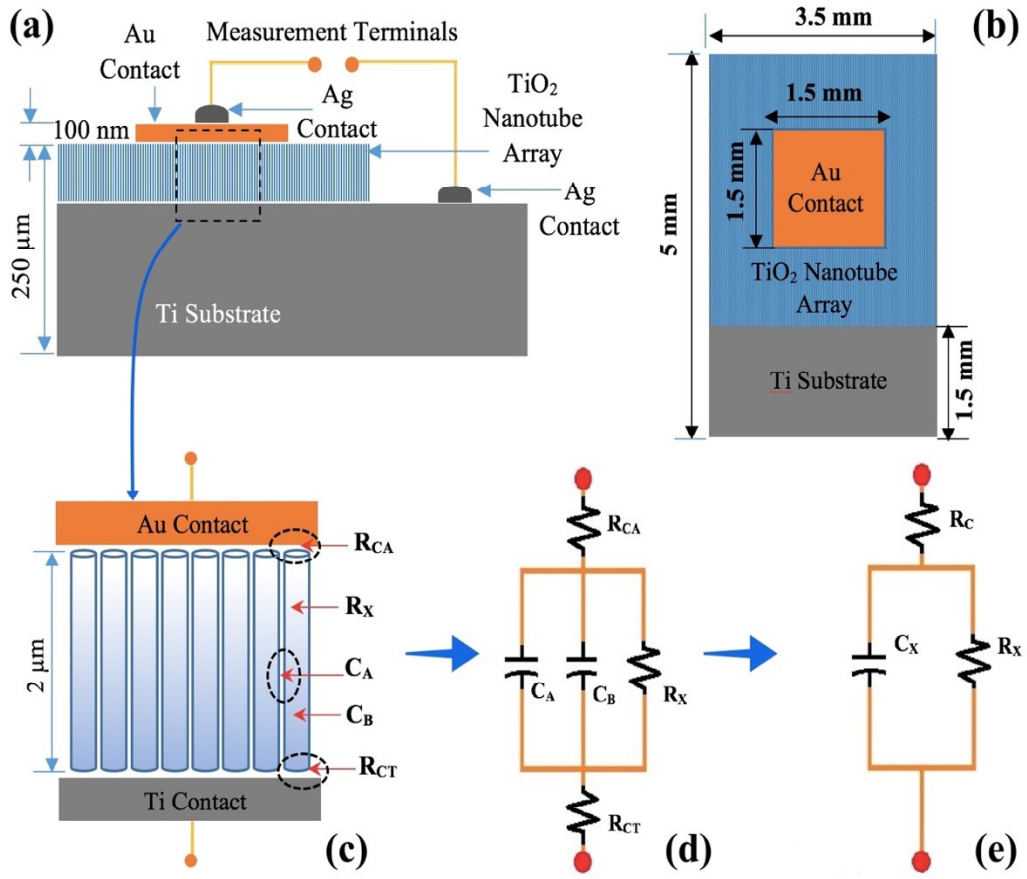

Fig. 2.3 (a) A schematic of TiO_2 nanotubes-based sandwich-type sensor device, (b) Top view of the sensor device, (c) Simplified device structure: Au/TiO_2 nanotubes/Ti, (d) Corresponding circuit model of the device, and (e) Simplified representation in Randle's circuit model. (Dimensions are not to scale)

empty space (within the pores and void region of TiO_2 nanotubes) and TiO_2 nanotubes, respectively. For the simplicity of model, depletion capacitances were ignored near the metal-semiconductor interface. The circuit model shown in Fig. 2.3 (d) has further simplified into Randle's circuit as depicted in Fig. 2.3 (e) where R_C represents the contact resistance, C_X is the device capacitance and R_X is the device resistance. Resistive component (R_X) originated from TiO_2 nanotubes can be modeled with its morphological parameters like inner diameter (2r), wall thickness (D) and tube length (L) as shown in Fig. 2.4 (a) and (b). Three assumptions have been considered for developing the electrical model. These assumptions are as follow: (i.) nanotubes are fully wall separated and free standing in nature, (ii.) uniform carrier concentration (N)

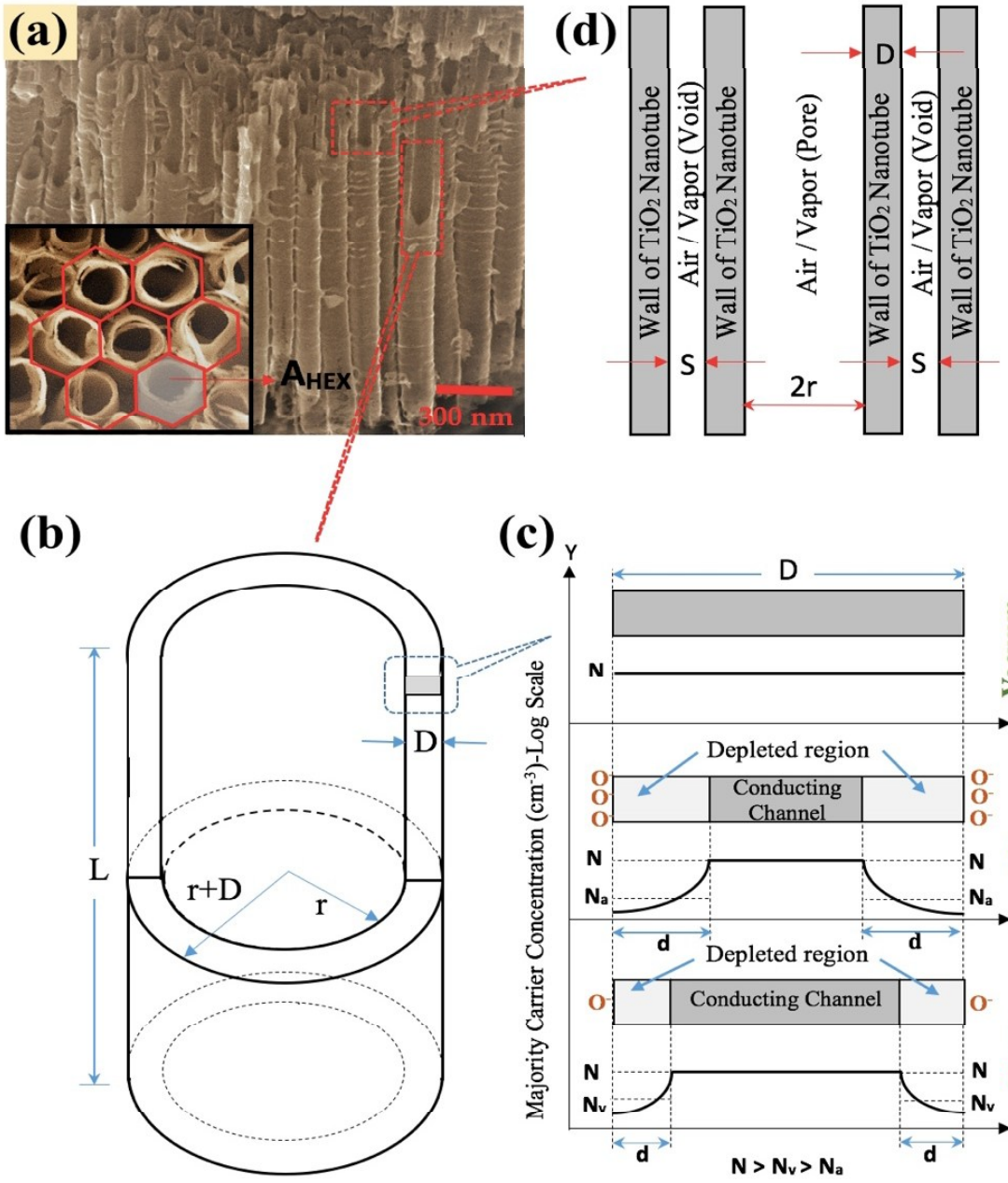

Fig. 2.4 Device modeling of TiO_2 nanotubes for deriving the resistive and capacitive components; (a) FESEM (side view) of nanotubes array. Top view is fitted in hexagonal grid geometry in inset, (b) A schematic of single TiO_2 nanotube showing morphological parameters, (c) majority carrier distribution in nanotubes wall in different ambient i.e. vacuum, air and reducing vapor, and (d) A schematic of the cross-sectional view of TiO_2 nanotubes for showing free space (pore and void region).

throughout the nanotubes, and (iii.) top surface of TiO_2 nanotubes array is highly uneven or roughly in nature and thickness of physically deposited Au top electrode is

very thin (~100 nm). So, a thin Au layer is not enough to mask the nanotube surface completely. Sufficient pores exist in Au/TiO_2 surface and target vapor comes to the contact of the inner and outer wall of TiO_2 nanotube. Based on these assumptions, R_X can be represented by eq. (2.9) [16].

$$R_X = \frac{R'_x}{n} = \frac{L}{nqN\pi(D-2d)(D+2r)\mu_n} \tag{2.9}$$

$$\text{where, } d = \sqrt{\frac{\varepsilon_0 \varepsilon_a kT}{q^2 N_{a/v}}} \tag{2.10}$$

R'_x can be considered as the resistance of an individual nanotube, n is the density of nanotubes (i.e. the number of nanotubes under contact area), μ_n is the mobility of TiO_2 (anatase) at temperature T, ε_a is the dielectric constant of TiO_2 (anatase), and N_a and N_v are the average carrier concentration on the surface (depleted region) of nanotubes in air and in reducing vapor ambient, respectively as shown in Fig. 2.4 (c). In ideal vacuum condition, R_x expression in eq. (2.9) can be modified by considering 2d=0. Resistive change of the nanotubes array principally depends on the thickness (D-2d) of the conducting channel (carrier concentration, N) in air and target vapor ambient. As, $(D\text{-}2d)_{vapor} > (D\text{-}2d)_{air}$, nanotubes resistance decreases in the presence of reducing vapor ambient compared to the air ambient.

Contact resistances, R_{CA} and R_{CT} were originated from Au/TiO_2 and Ti/TiO_2 interface, respectively. However, based on the work function of metals used in the device (Ti = 4.33 eV and Au = 5.3 eV) and electron affinity of TiO_2 (anatase = 5.10 eV), the Ti/TiO_2 junction should behave like an ohmic contact offering very small contact resistance (R_{CT}) compared to the Au/TiO_2 junction (R_{CA}). Contact resistance of the metal-semiconductor Schottky junction (R_C) can be represented on the basis of thermionic emission theory as in eq. (2.11) [17, 18].

$$R_C = \frac{R'_C}{n} = \frac{kT}{nqI} \tag{2.11}$$

$$I = I_c \left[\exp\left(\frac{qV}{kT}\right) - 1\right] \tag{2.12}$$

$$I_0 = A_{NT} R^* T^2 \exp\left(-\frac{q\Phi_b}{kT}\right) \tag{2.13}$$

R'_C can be considered as the contact resistance between metal and single nanotubes junction. n is the total number of TiO_2 nanotubes under the contact area. A_{NT} is the cross-sectional area of single TiO_2 nanotube [$A_{NT}=\pi D(D+2r)$], Φ_b represents the barrier height of Au/TiO_2 junction and R^* is the Richardson constant.

To model the capacitive components of the device, C_A and C_B, TiO_2 nanotubes array were fitted in a hexagonal grid geometry (Fig. 2.4 (a)). Free space in TiO_2 nanotubes array is defined by subtracting the cross-sectional area of single nanotubes [$A_{NT}=\pi D(D+2r)$] from the total area of a hexagon (A_{HEX}). A_{HEX} can also be represented with nanotubes' parameters as $2\sqrt{3}(r+D+0.5S)^2$, where S is the average wall separation as shown in Fig. 2.4 (d) [19]. Now, the total capacitance C_X can be represented as the parallel of C_A and C_B as shown in eq. (2.14).

$$C_x = n(C_A + C_B) = \frac{n\varepsilon_0}{L}[(A_{HEX} - A_{NT})\,\varepsilon_v + A_{NT}\,\varepsilon_a] \tag{2.14}$$

Where, n represents total number of TiO_2 nanotubes under contact area and ε_v is the dielectric constant of target VOC. Surface reaction of reducing vapor releases free electrons to the nanotubes surface lowering the depletion width (d) as well as nanotubes resistance (R_X). Resistive sensitivity/RRM of the TiO_2 nanotubes-based sensor can be represented in eq. (2.15) based on eq. (2.9).

$$RRM = \frac{2[d(N_a) - d(N_v)]}{D - 2d(N_a)} \tag{2.15}$$

Resistive response of the sensor shown in eq. (2.15) principally depends on the depletion width (d) which is a function of surface carrier concentration at different ambient like air (N_a) and vapor (N_v). Resistive response of Au/TiO_2 nanotubes/Ti sensor can be improved effectively by lowering the nanotubes wall thickness (D). In presence of a reducing vapor, free space capacitance (C_A) was increased because reducing vapors possess higher relative permittivity than air; thus, increasing the total capacitance (C_X) of Au/TiO_2 nanotubes/Ti device. Capacitive sensitivity/ CRM of TiO_2 nanotubes-based sensor can be represented as eq. (2.16) based on eq. (2.14) by

considering the dielectric constant of air as 1 [20].

$$\text{CRM} = \frac{(A_{HEX} - A_{NT})(\varepsilon_v - 1)}{(A_{HEX} + A_{NT})(\varepsilon_a - 1)} \tag{2.16}$$

Capacitive response/CRM of the sensor (eq. (2.16)) primarily depends on the dielectric value of target vapor (ε_v) and increases in case of target VOCs having higher values of dielectric constant. CRM may also improve if free space in the sensing layer (i.e. A_{HEX}-A_{NT} for TiO_2 nanotubes) increases as VOC molecules can diffuse more easily in empty free space. Capacitive response also depends on the dielectric constant of sensing material (anatase TiO_2) and CRM of the sensor can be increased for the sensing materials having a lesser magnitude of dielectric constant.

2. 5 Impedance analysis of TiO_2 nanotubes-based sensor

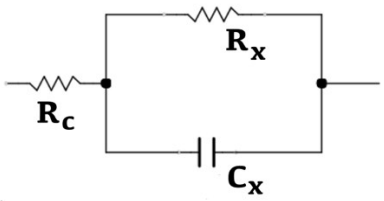

Fig. 2.5 Equivalent electrical circuit of fabricated Au/TiO_2 nanotubes/Ti sensor.

Cole-Cole plot is a graphical representation of real (Re (Z) on the horizontal axis) and imaginary (Im (Z) on the vertical axis) components of the device impedance for a range of frequencies. This plot is helpful in determining the values of individual electrical parameters of the device. In case of a semi-circular Cole-Cole plot whose minimum x-intercept value passes through the origin, the equivalent circuit can be modeled as a parallel combination of resistance (R_X) and capacitance (C_X). The maximum value of x-intercept gives the value of R_X and C_X can be determined using relation $\omega_{max} = 1/R_X C_X$ where ω_{max} represents the value of angular frequency at maximum magnitude of Im Z. If semi-circle is shifted horizontally towards positive x-axis, then it can be interpreted that the equivalent circuit consists of a serial resistance

(R_c) with a parallel combination of above discussed R_X and C_X. The magnitude of the horizontal shift of x-intercept minima from origin gives the value of R_X. The corresponding equivalent circuit diagram of a horizontally shifted semi-circle in a Cole-Cole plot is given in Fig. 2.5 which is similar to Fig. 2.3 (e) that was used to model the equivalent electrical circuit of the sensor.

2. 5. 1 Effect of temperature

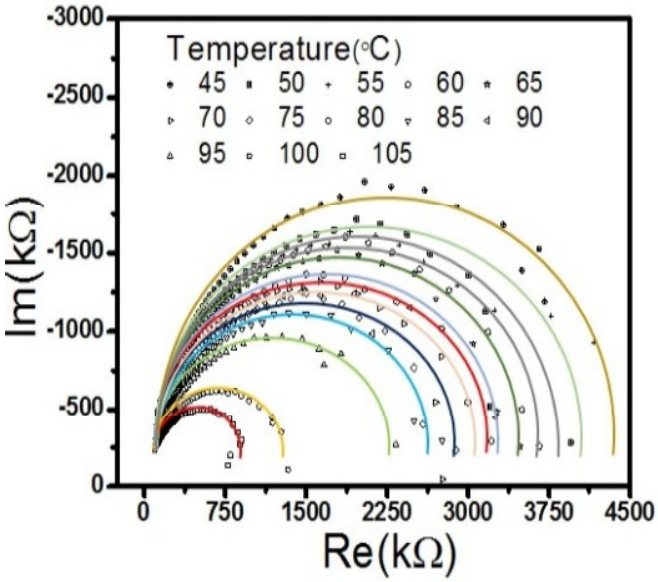

Fig. 2.6 Impedance variation (or Nyquist plot) of Au/TiO_2 nanotubes/Ti device at variable temperature (45 °C to 105 °C) in air ambient.

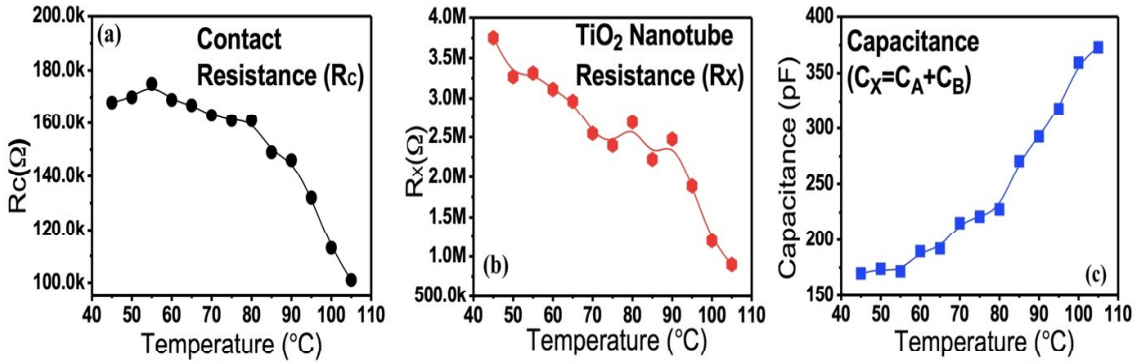

Fig. 2.7 Effect of temperature on various device components like (a) contact resistance (R_C), (b) device resistance (R_X), and (c) device capacitance (C_X).

The effect of temperature on resistive and capacitive components of Au/TiO_2 nanotubes/Ti device was tested in air ambient. Impedance behavior (Nyquist plot) of the device was observed at moderate temperature range of 45 °C to 105 °C as shown in Fig. 2.6. Semicircle radius was decreased with the increase of temperature that signifies the lowering of device resistance at a higher temperature at air ambient. Temperature effect on individual device components i.e. R_C, R_X and C_X were calculated from Fig. 2.6 and represented in Fig. 2.7 (a-c).

Contact resistance (R_C) shows an insignificant change when the temperature was kept in the range of 45 - 80 °C but started to decrease beyond 80 °C maintaining the rate of around 10 kΩ/5 °C as shown in Fig. 2.7 (a). Temperature dependency of the contact resistance, R_C is shown in eq. 2.5. Resistance of nanotubes (R_X) decreases from 4 MΩ to 1 MΩ when the temperature was kept in the range of 45 - 105 °C as shown in Fig. 2.7 (b). At higher temperatures, N increases due to thermal generation which is responsible for the lowering of R_X (eq. (2.5)).

Capacitive component C_X (i.e. C_A+C_B) was increased with temperature as shown in Fig. 2.7 (c). As C_A was originated from free space (air ambient) of TiO_2 nanotubes array (eq. (2.10)), no significant changes can be expected due to temperature increment. However, C_B was originated from solid TiO_2 nanotubes, and thus responsible for incremental behavior of C_X with temperature. The dielectric constant of the ionic solid like TiO_2 significantly influenced by its ionic displacement and that eventually effects the electronic polarizations [21]. Ionic displacement becomes stronger when metal and oxygen ions are weakly bonded and carrying large electric charges in the metal oxide. As ions and ionic polarization both get increase with temperature, dielectric constant as well as capacitance value of the ionic solid like TiO_2 increases with temperature.

Thus, the operating temperature was found to be an important parameter for both the resistive and capacitive sensing. Surface adsorption increases up to some extent with temperature offering higher value of resistive response magnitude but after

an optimal temperature, the desorption process also comes into picture which effectively reduces the response magnitude. Also, at the higher temperature, $\mathcal{E}_a$ may increase for ionic solids like anatase TiO_2 and with reference to eq. (2.10), and thus capacitive response gets reduced.

2. 5. 2 Effect of vacuum

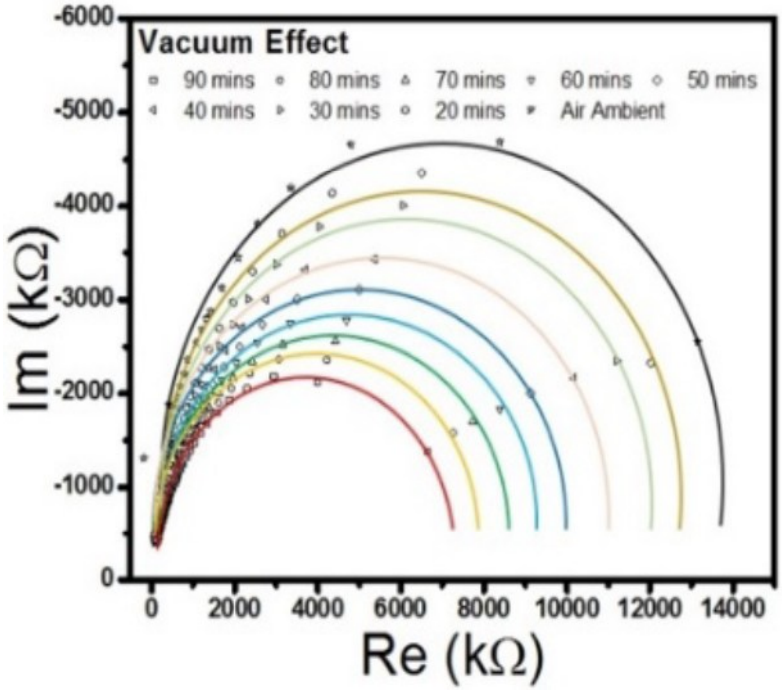

Fig. 2.8 Impedance variation of Au/TiO_2 nanotubes/Ti device in air ambient to vacuum condition reached after 20 min to 90 min at 30 °C.

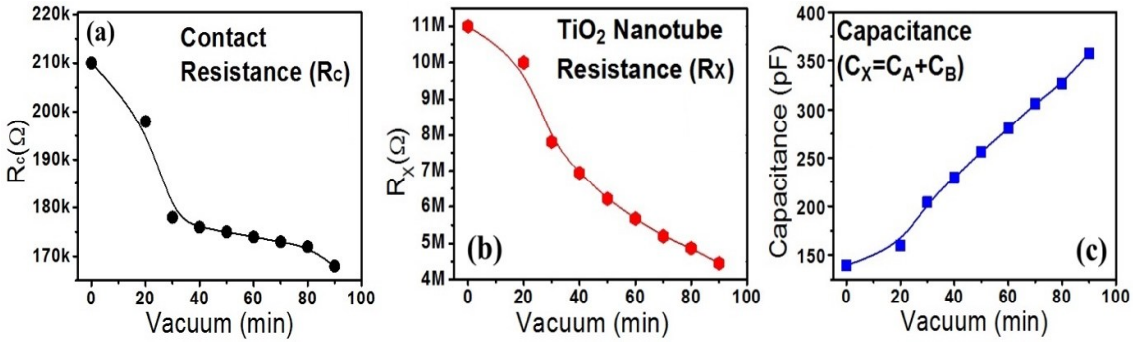

Fig. 2.9 Effect of vacuum on various device components like (a) contact resistance (R_C), (b) device resistance (R_X), and (c) device capacitance (C_X).

Impedance analysis in the vacuum ambient shows the potentiality of the sensor under resistive mode. In air ambient, oxygen species like O^-, O^{2-}, etc. get adsorbed chemically on the surface of TiO_2 nanotubes which lowers the free electron concentration. In vacuum, due to the desorption of oxygen ions from TiO_2 surface, depletion thickness gets (d) decreased which lowers the resistance of the nanotubes as shown in eq. (2.5). Impedance analysis as presented in Fig. 2.8 showing the vacuum effect on the sensor. Individual device component i.e. R_C, R_X and C_X were calculated from Fig. 2.8 and represented in Fig. 2.9 (a-c). The resistance of nanotubes (R_X) decreases from 11 MΩ to 4 MΩ as the vacuum condition is maintained from ambient condition to 90 mins as shown in Fig. 2.9 (b) which validate the potentiality of the sensor to work in resistive mode.

2. 5. 3 Effect of reducing ambient

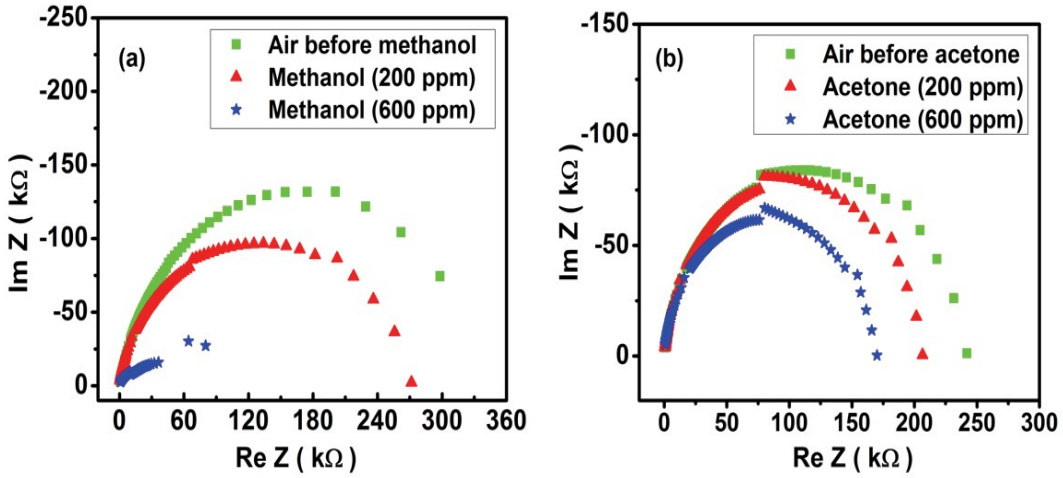

Fig. 2.10 Cole-Cole plots of Au/TiO_2 nanotubes/Ti device in (a) methanol ambient, and (b) acetone ambient.

Cole-Cole plot of the sensor operated at 27 °C for different concentrations of reducing ambient like methanol (200 and 600 ppm) is given in Fig. 2.10 (a). It can be envisaged from Fig. 2.10 (a) that the impedance spectrum of the sensor in methanol ambient differs from that of air ambient. Also, plots are semi-circular in nature, and

thus the sensor can be modeled using Fig. 2.5 as discussed above. The radius of the semicircle reduces when ambient of the sensor changes from air to 200 ppm methanol and it gets further reduced when the concentration of methanol increases from 200 ppm to 600 ppm. This shows that the resistance of the device (R_X) reduces with an increase in methanol concentration. This outcome can be explained using surface kinetics. Oxygen molecules from air ambient get adsorb on n-type TiO_2 nanotubes surface and remain in the active state (O^-) on the surface. When reducing vapors like methanol interact with these active sites, they get oxidize and electrons are generated in these reactions which effectively increases the majority carrier concentration and hence a reduction in the resistance of TiO_2 sensing layer was observed [22]. On the other hand, the capacitance value of the device increases as the amount of methanol concentration increases. When pores and void regions of the nanotubes array get filled with vapor molecules, it effectively changes the dielectric constant of the sensing layer. As dielectric constant of free space (or air) is usually considered as unity and dielectric constant value of vapors are always more than unity, hence effective dielectric constant value gets increased in presence of vapors resulting in an increment in capacitance value [23].

Similarly, the study of the impedance of the sensor was done in another reducing ambient of acetone and Cole-Cole plot of the sensor for different concentrations of acetone (200 and 600 ppm) at 27 °C is given in Fig. 2.10 (b). It can be noticed from the plot that the amount of reduction in semicircle diameter is relatively less in the case of acetone ambient. This indicates that sensor resistance reduced with a lesser rate in the case of acetone than in the case of methanol. The downward shift of the peak values of Im Z data as ambient of the sensor get changed from air ambient to 200 ppm of acetone ambient and then to 600 ppm of acetone ambient is also less profound in case of acetone plot relative to methanol plot. Thus, qualitatively, it means that the capacitance of the sensor increases with a lesser rate in the case of acetone than in the case of methanol.

2. 6 Conclusions

This study identified various resistive and capacitive components of 1-D TiO_2 nanostructures-based sensor. The sensor was developed by synthesizing TiO_2 nanotubes using electrochemical anodization of Ti foil. Au and were used as the top and bottom electrodes, respectively. The proposed electrical circuit model of the sensor consists of the following components: (i.) R_C as the contact resistance, (ii.) C_X as the device capacitance, and (iii.) R_X as the device resistance. These individual circuit components were modeled with the help of structural and morphological parameters of TiO_2 nanotubes. The device model was then verified by measuring the impedance of the sensor at variable temperature, different vacuum condition and in reducing vapor ambient. Au/TiO_2 nanotubes/Ti device proved its suitability to be used as both resistive and capacitive sensor. Also, the sensor can be tuned towards more resistive or more capacitive change by controlling the structural and morphological parameters of TiO_2 nanotubes array.

References

1. L.L. Wang, H.Y. Wang, W.C. Wang, K. Li, X.C. Wang, X.J. Li, Capacitive humidity sensing properties of ZnO cauliflowers grown on silicon nanoporous pillar array, Sensors and Actuators B 177 (2013) 740-744.
2. A. Hazra, B. Bhowmik, K. Dutta, V. Manjuladevi, R.K. Gupta, P. Bhattacharyya, Low temperature methanol sensing by p-type nano-titania: correlation with defects states and Schottky Barrier model, IEEE Trans. Nanotechnology 14 (2015) 187-195.
3. H. Wang, B. Kang, F. Ren, L. Tien, P. Sadik, D. Norton, S. Pearton, J. Lin, Hydrogen-selective sensing at room temperature with ZnO nanorods, Applied Physics Letters 86 (2005) 243503.
4. Y. Kwon, H. Kim, S. Lee, I. Chin, T. Seong, W. Lee, C. Lee, Enhanced ethanol sensing properties of TiO_2 nanotube sensors, Sensors and Actuators B 173 (2012) 441-446.
5. L.Y. Li, Y.F. Dong, W.F. Jiang, H.F. Ji, X.J. Li, High-performance capacitive humidity

sensor based on silicon nanoporous pillar array, Thin Solid Films 517 (2008) 948-951.

6. A.S. Zuruzi, A. Kolmakov, N.C. MacDonald, M. Moskovits, Highly sensitive gas sensor based on integrated titania nanosponge arrays, Applied Physics Letters 88 (2006) 102904.
7. A. Hazra, S. Das, J. Kanungo, C.K. Sarkar, S. Basu, Studies on a resistive gas sensor based on sol–gel grown nanocrystalline p-TiO_2 thin film for fast hydrogen detection, Sensors and Actuators B 183 (2013) 87-95.
8. S. Singh, H. Kaur, V.N. Singh, K. Jain, T.D. Senguttuvan, Highly sensitive and pulse-like response toward ethanol of Nb doped TiO_2 nanorods based gas sensors, Sensors and Actuators B 171–172 (2012) 899-906.
9. Z. Ling, C. Leach, The effect of relative humidity on the NO_2 sensitivity of a SnO_2/WO_3 heterojunction gas sensor, Sensors and Actuators B 102 (2004) 102-106.
10. S. Roy, C. Jacob, S. Basu, Studies on Pd/3C-SiC Schottky junction hydrogen sensors at high temperature, Sensors and Actuators B 94 (2003) 298-303.
11. H. Taghinejad, M. Taghinejad, M. Abdolahad, A. Saeidi, S. Mohajerzadeh, Fabrication and modeling of high sensitivity humidity sensors based on doped silicon nanowires, Sensors and Actuators B 176 (2013) 413-419.
12. N.M. Kiasari, S. Soltanian, B. Gholamkhass, and P. Servati, Room temperature ultra-sensitive resistive humidity sensor based on single zinc oxide nanowire, Sensors and Actuators A 182 (2012) 101–105.
13. P. Roy, S. Berger, P. Schmuki, TiO_2 nanotubes: synthesis and applications, Angewandte Chemie International Edition 50 (2011) 2904-2939.
14. Y. Liu, L. Wang, H. Wang, M. Xiong, T. Yang, G.S. Zakharova, Highly sensitive and selective ammonia gas sensors based on PbS quantum dots/TiO_2 nanotube arrays at room temperature, Sensors and Actuators B 236 (2016) 529-536.
15. A. Hazra, K. Dutta, B. Bhowmik, P. Bhattacharyya, Highly repeatable low-ppm ethanol sensing characteristics of p-TiO_2-based resistive devices, IEEE Sensors 15 (2015) 408-416.
16. A. Hazra, B. Bhowmik, K. Dutta, P. P. Chattopadhyay, P. Bhattacharyya, Stoichiometry, length, and wall thickness optimization of TiO_2 nanotube array for efficient alcohol sensing, ACS Appl. Mater. Interfaces 7 (2015) 9336–9348.

17. I. Dökme, S. Altindal, On the intersecting behaviour of experimental forward bias current–voltage (I–V) characteristics of Al/SiO_2/p-Si (MIS) Schottky diodes at low temperatures, Semiconductor Science and Technology 21 (2006) 1053–1058.

18. S. Chand, On the intersecting behaviour of current voltage characteristics of inhomogeneous Schottky diodes at low temperatures, Semiconductor Science and Technology 19 (2004) 82–86.

19. K. Dutta, A. Hazra, P. Bhattacharyya, Ti/TiO_2 nanotube array/Ti capacitive device for non-polar aromatic hydrocarbon detection, IEEE Trans. Device and Materials Reliability 16 (2016) 235–242.

20. M.P. López-Sancho, L. Brey, Temperature dependence of the dielectric constant and resistivity of diluted magnetic semiconductors, Phys. Rev. B, Condens. Matter. 68 (2003) 113201.

21. B. Tareev, A. Troitsky, Physics of Dielectric Materials, Mir Moscow Second Edition 1975.

22. B. Comert, N. Akin, M. Donmez, S. Saglam, S. Ozcelik, Titanium dioxide thin films as methane gas sensors, IEEE Sensors 16 (2016) 8990-8996.

23. E.S. Snow, F.K. Perkins, E.J. Houser, S.C. Badescu, T.L. Reinecke, Chemical detection with a single-walled carbon nanotube capacitor, Science 307 (2005) 1942-1945.